Available online at www.sciencedirect.com

ScienceDirect

Journal of Magnesium and Alloys 2 (2014) 116–123
www.elsevier.com/journals/journal-of-magnesium-and-alloys/2213-9567

Full length article

Strain-hardening and warm deformation behaviors of extruded Mg–Sn–Yb alloy sheet

Jing Jiang [a], Guangli Bi [b], Guoyong Wang [a], Qing Jiang [a], Jianshe Lian [a], Zhonghao Jiang [a,*]

[a] *Key Laboratory of Automobile Materials, College of Materials Science and Engineering, Jilin University, Nanling Campus, Changchun 130025, China*
[b] *State Key Laboratory of Advanced Processing and Recycling of Nonferrous Metals, Lanzhou University of Technology, Lanzhou 730050, China*

Received 25 January 2014; revised 27 April 2014; accepted 13 May 2014
Available online 28 June 2014

Abstract

Strain-hardening and warm deformation behaviors of extruded Mg–2Sn–0.5Yb alloy (at.%) sheet were investigated in uniaxial tensile test at temperatures of 25–250 °C and strain rates of 1×10^{-3} s^{-1}–0.1 s^{-1}. The data fit with the Kocks–Mecking type plots were used to show different stages of strain hardening. Besides III-stage and IV-stage, the absence of the II-stage strain hardening at room temperature should be related to the sufficient dynamic recrystallization during extrusion. The decrease of strain hardening ability of the alloy after yielding was attributed to the reduction of dislocation density with increasing testing temperature. Strain rate sensitivity (SRS) was significantly enhanced with increasing temperature, and the corresponding *m*-value was calculated as 0.07–0.12, which indicated that the deformation mechanism was dominated by the climb-controlled dislocation creep at 200 °C. Furthermore, the grain boundary sliding (GBS) was activated at 250 °C, which contributed to the higher SRS. The activation energy was calculated as 213.67 kJ mol^{-1}, which was higher than that of lattice diffusion or grain boundary self-diffusion. In addition, the alloy exhibited a quasi superplasticity at 250 °C with a strain rate of 1×10^{-3} s^{-1}, which was mainly related to the fine microstructure and the presence of the Mg_2Sn and $Mg_2(Sn,Yb)$ particles.
Copyright 2014, National Engineering Research Center for Magnesium Alloys of China, Chongqing University. Production and hosting by Elsevier B.V. Open access under CC BY-NC-ND license.

Keywords: Mg–Sn–Yb alloy sheet; Strain hardening; Strain rate sensitivity; Activation energy

1. Introduction

Research on Magnesium and Magnesium alloys has been received more attention due to their excellent properties such as low density, high specific strength and good casting properties and mechanical properties [1]. Magnesium and its alloys have poor formability at room temperature because of its hexagonal closed-packed (h.c.p.) structure [2,3]. This greatly restricts the development and application of Mg alloys in some press forming fields. Therefore, at present, most of Mg alloys are casting and/or die casting components [4–6].

The deformation behavior of Mg alloys with h.c.p. structure is more complex than Al alloys (f.c.c.) and Fe alloys (b.c.c.), because the h.c.p. structure has low symmetry, few slip systems and strong plastic anisotropy [7]. Usually, the dominant slip system of Mg alloys is basal one at room temperature. The homogeneous deformation of polycrystals is possible, if five independent slip systems are activated according to the von Mises criterion. The number of independent mode of the basal slip is only two for Mg alloys, which does not reach five, and thus the non-basal slip should be activated [8]. The activity of non-basal slip systems is related to critical resolved shear stress (CRSS), which mainly depends on temperature and/or

* Corresponding author. Tel./fax: +86 431 85095876.
E-mail address: jiangzhonghaovip@163.com (Z. Jiang).
Peer review under responsibility of National Engineering Research Center for Magnesium Alloys of China, Chongqing University

Production and hosting by Elsevier

http://dx.doi.org/10.1016/j.jma.2014.05.004.
2213-9567/Copyright 2014, National Engineering Research Center for Magnesium Alloys of China, Chongqing University. Production and hosting by Elsevier B.V. Open access under CC BY-NC-ND license.

strain rates. The CRSS for Mg alloys rapidly decreases with increasing temperature and decreasing strain rate [8,9]. Consequently, it can be known that the temperature and strain rate significantly influence the deformation behavior of Mg alloys. The deformation behavior of Mg alloys is generally discussed in terms of softening and hardening processes. Some metallurgical phenomena may simultaneously occur during these processes such as strain-hardening, dynamic recovery and dynamic recrystallization (DRX), resulting in the changes in the microstructure and mechanical properties. Strain-hardening behavior is also one of important considerations in evaluating plastic deformation of materials [10–12]. The strain hardening ability is mainly related to the resistance to dislocation slip by the second-phase particles [13], high-angle grain boundaries [10] and twining boundaries [10,14,15]. In addition, a recent report showed that the strong strain-hardening effect in ZrCuAlNiO alloy was believed to result from a transformation from ZrCu phase to Martensite phase [16]. At present, the strain-hardening behaviors of some as-cast and wrought Mg alloys, such as ZE41, QE22, AZ31, Mg–Y–Zn, Mg–Al–Sn and Mg–Li alloys have been investigated [9].

Recently, Mg–Sn based alloys, as new type heat resistant Mg alloy systems, have been attended by many researchers. According to the Mg–Sn binary phase diagram, it can be known that Sn has a larger solubility in α-Mg and its solubility limit is 14 wt.% at a eutectic temperature of 561 °C. Also, the Mg_2Sn phase has higher thermally stability due to its high melting point (770 °C) [17]. Therefore, the addition of Sn as a major alloying element can effectively improve heat resistant properties of Mg alloys by solution strengthening and second phase strengthening. Moreover, the addition of the third alloying elements X (X = Ca, Sb, Al, Bi, Mn and Y et al.) can further effectively strengthen the creep resistant of Mg–Sn alloy by adjusting the volume fraction of Mg_2Sn phase and precipitating new Mg–Sn–X phase with high thermal stability [18–23]. Besides, the presence of these phases possibly make the Mg–Sn based alloys generate an obvious strain hardening behavior by creating dislocation pile-ups or obtain good high temperature plasticity even superplaticity by inhibiting grain boundary sliding to retard grain growth. More recently, hot deformation behaviors of as-cast Mg–2Sn–2Ca alloy and Mg–3Sn–2Ca–0.4Al alloy have been investigated by constructing processing maps [24–26]. The corresponding experimental results indicate that the high appear activation energy is mainly attributed to the generation of back stress by CaMgSn intermetallic particles. Kim et al. [23] have also reported the high deformation behavior of hot-rolled Mg-1.5 at.%Sn(0.8 at.%Zn) alloy sheets. The investigation demonstrates that the Zn addition makes the elongation to failure of the alloy reach 310% at a strain rate of 1×10^{-3} s^{-1} at 350 °C. In addition, the low temperature superplasticity of extruded Mg–8Sn–1Al–1Zn alloy has been reported by Park et al. [27], and the study shows that the alloy exhibits a tensile elongation of 410–950% at strain rates in range 1×10^{-3}–1×10^{-4} s^{-1} at 200 °C. The superplasticity of the alloy mainly results from the fine microstructure and the precipitation of stable Mg_2Sn particles. As mentioned above, the Mg–Sn alloy containing rare earth (RE) elements should exhibit good heat resistant, strain hardening and high temperature deformation behavior due to the high solubility limit of RE elements in α-Mg matrix and the precipitation of good thermally stable Mg–Sn–RE phase. Up to now, most investigations mainly focus on the microstructure and mechanical properties of extruded Mg–Sn–RE(La, Di and Y) alloys [19,28,29]. However, there have been few reports on strain hardening and warm deformation behavior of the extruded Mg–Sn–RE alloy, especially for extruded Mg–Sn–Yb alloy sheet. Therefore, based our previous work [30], in this paper, the extruded Mg–Sn–Yb alloy sheet was prepared and its strain-hardening behavior was evaluated using Kocks–Mecking phenomenological approach [7,31], and the warm deformation behavior of the alloy sheet was also investigated.

2. Experimental procedures

A normal Mg–2Sn–0.5Yb alloy sheet (at.%) was prepared from pure magnesium (99.50 wt.%), pure tin (99.98 wt.%) and Mg-20 wt.%Yb master alloys, which were melted in an iron crucible under the protection of antioxidant flux. The alloy melt was stirred to ensure composition homogeneity and held at about 720 °C for about 30 min, then was transferred into a semi-continuous casting machine at about 650 °C and finally cast into a billet of 90 mm in diameter and 500 mm in length. The billet was machined into a diameter of 82 mm then extruded into the sheet with a thickness of 5 mm and a width of 80 mm by an extrusion ratio of 17 at 360 °C.

The microstructures of the alloy were characterized by optical microscopy (OM) and scanning electron microscopy (SEM) with energy dispersion spectrometry (EDS)(JSM-5600) and High-resolution transmission electron microscopy (HRTEM)(JEM-2011F). Specimens for the SEM observation were ground by using different sand papers and polished, then etched in a solution with a solution of 30 ml acetic acid+15 ml water+6 g picric acid+100 ml ethanol. The average grain size of the alloys was measured by the linear intercept method. Tensile tests were performed in an Instron-type tensile testing machine (Instron 1211) at room temperature, 200 °C and 250 °C, respectively, with the strain rate range from 1×10^{-3} s^{-1} to 1×10^{-1} s^{-1}. The gauge size of the tensile specimens is 15.0 mm × 3.0 mm × 2.5 mm. Before the tensile tests at elevated temperatures, the tensile specimens were hold for 6 min to make temperature uniform. The fractured surfaces of the tensile specimens were examined by using SEM.

3. Results

3.1. Microstructure

The microstructure of as-cast and extruded alloys is shown in Fig. 1. The microstructure of as-cast alloy is mainly composed of a great number of dendritic crystals and particles distributed in the dendtritic boundaries (see Fig. 1(a)). These

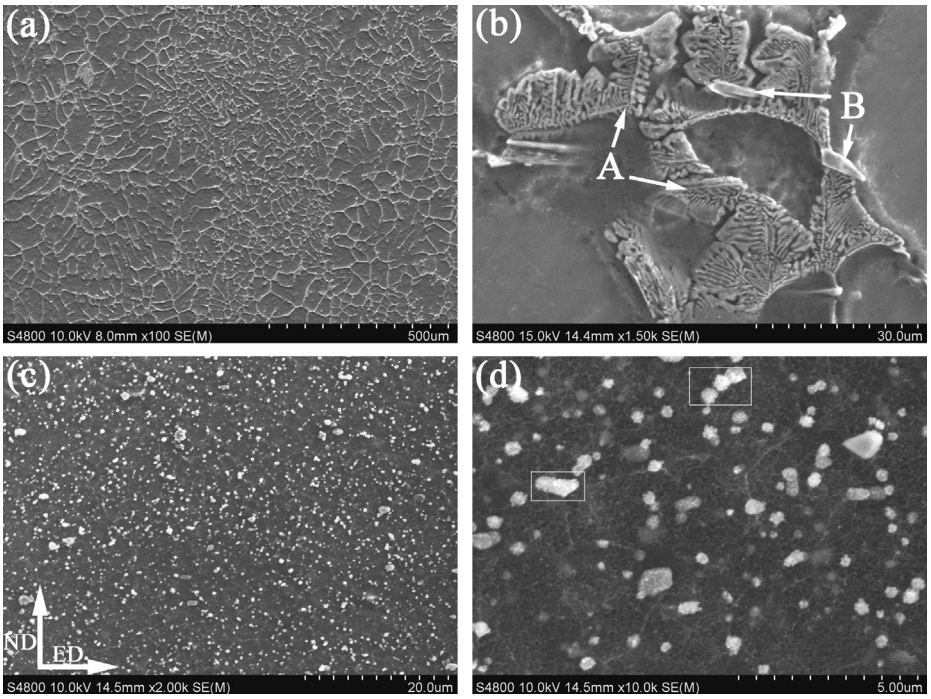

Fig. 1. Microstructures of the alloy in the as-cast state (a), (b) and extruded sheet state (c), (d), the low-magnification images are (a) and (c), the high-magnification images are (b) and (d), respectively.

particles mainly consist of typical fish-bone shaped eutectic phase (marked as A) and strip-type phase (marked as B) with about 10 μm in length and 2 μm in width (see Fig. 1(b)). According to the previous XRD and EDS results [30], these particles are identified to be Mg_2Sn phase and $Mg_2(Sn,Yb)$ phase, respectively. After the extrusion, these particles crush and dispersedly distribute along the extruded direction (see Fig. 1(c)). It is noted that some particle clusters are observed as marked by the white frame in Fig. 1(d). These clusters include a dense mass of the fine nanometer-scale particles, which was not reported in other Mg alloys. In addition, the grain size significantly decreases due to the role of dynamic recrystallization and the average grain size was measured to be about 5 μm.

3.2. Tensile properties

The stress-strain curves of the alloy obtained from the uniaxial tensile tests at different temperatures and different strain rates are plotted in Fig. 2. At room temperature, the flow stress increases and the elongation to failure decreases slightly with increasing strain rate. At elevated temperatures, the flow stress decreases rapidly and the elongation to failure increases significantly as compared with those at room temperature, and both the flow stress and the elongation to failure show significant dependence on strain rate. In order to evaluate the strain hardening ability of the alloy and the effect of temperature and strain rate on the uniform plastic deformation, the strain hardening exponent n in the well-known empirical Hollomon equation $\sigma_T = K\varepsilon_T^n$ was measured using the true stress-strain (σ_T–ε_T) data in the uniform plastic deformation stage, where K is the material coefficient. The double logarithmic $\log\sigma_T$–$\log\varepsilon_T$ curves in Fig. 3 indicate that the strain hardening behavior of the alloy follows well the Hollomon equation in the range of the uniform plastic deformation. The derived values of n (the slopes of the $\log\sigma_T$–$\log\varepsilon_T$ curves) at different temperatures and different strain rates are listed in Table 1. As shown, the n value increases with increasing strain rate at room temperature and is approximately consistent with the uniform plastic strain ε_u, i.e. $n \approx \varepsilon_u$ at different strain rates. While at elevated temperatures, the n value decreases with increasing strain rate and is far smaller the corresponding uniform plastic strain. The above results of the n values indicate that the strain hardening ability of the alloy increases as strain rate increases at all temperatures, but decreases as temperature increases.

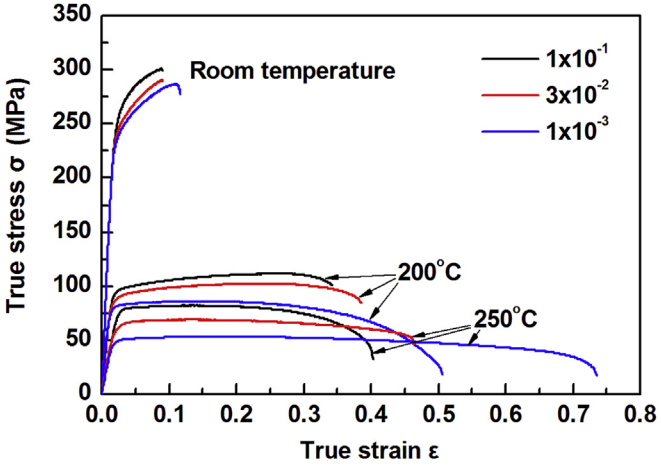

Fig. 2. Flow curves of the alloy at various temperatures and strain rates.

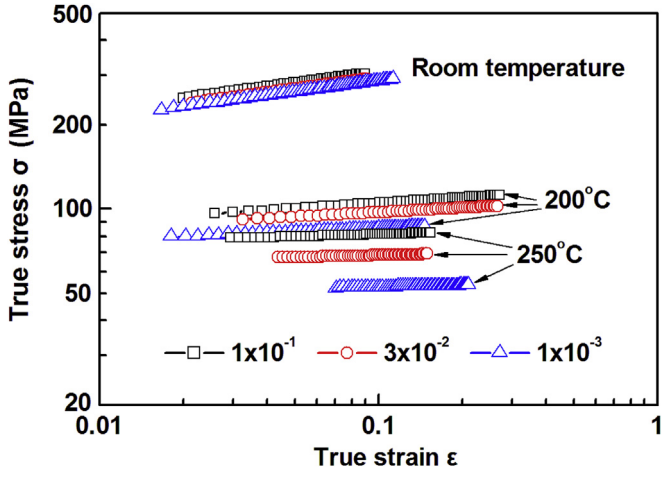

Fig. 3. Strain hardening curves of the alloy fitted from the tensile date.

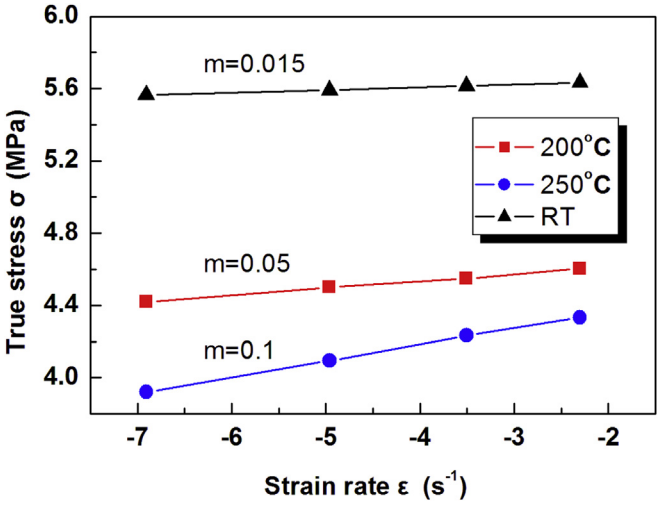

Fig. 4. Effects of temperature on strain rate sensitivity (m) of the flow stress at a true strain of 3% in the alloy.

3.3. Strain hardening rate

According to the Kocks–Mecking type [7], the curves of the strain hardening rate ($\Theta = d\sigma/d\varepsilon$)at room temperature, 200 °C and 250 °C are plotted in Fig. 5, respectively, as a function of the net flow stress ($\sigma-\sigma_{0.2}$). It is noted that the variations of Θ with temperature and strain exhibit a similar trend to that of n, e.g. the value of Θ decreases with increasing temperature and decreasing strain rate. At room temperature, the initial value of Θ is about 3000 MPa for the alloy at three strain rates (1×10^{-3} s^{-1}, 1×10^{-2} s^{-1} and 0.1 s^{-1}) (see Fig. 5). Notably, the Θ value does not exhibit a certain value after the yield stress. This indicates that there is not the II-stage hardening behavior in the Kocks-Mecking model. At 200 °C and 250 °C, the Θ value rapidly decreases with increasing $\sigma-\sigma_{0.2}$, thereby exhibiting the III-stage hardening behavior. The Θ value becomes small, and the IV-stage hardening behavior occurs at higher $\sigma-\sigma_{0.2}$. The typical III-stage and IV-stage hardening behaviors also occur at 250 °C (see insert in Fig. 5). The initial Θ value and the decreasing rate of Θ decrease with increasing temperature.

3.4. Strain rate sensitivity

In order to evaluate the sensitivity of the plastic deformation or flow stress to strain rate, the strain rate sensitivity exponent m in the well-known power law relation $\sigma_T = K'\dot{\varepsilon}_T^m$ was measured at the true strain of 3%, where K' is the material coefficient. From the double-logarithmic log σ_T − log$\dot{\varepsilon}_T$ curves in Fig. 4, the m values of the alloy were determined to be 0.015, 0.05 and 0.1 at room temperature, 200 °C and 250 °C, respectively. The significant decrease of the m value at room temperature as compared with those at elevated temperatures indicates a transition of the plastic deformation mechanism with increasing temperature. In addition, to further understand deformation mechanism of the alloy at elevated temperatures, the following constitutive equation describing the steady-state flow behavior can be used [32]

$$\dot{\varepsilon} = A\sigma^{n'} \exp\left(-\frac{Q}{RT}\right) \tag{1}$$

where A is a constant, n' is the stress exponent ($n' \approx 1/m$),R is the gas constant, T is the absolute temperature and Q is the apparent activation energy and can be given by

$$Q = R\left(\frac{\partial(\ln\sigma)}{\partial\ln(1/T)}\right)_{\dot{\varepsilon}}\left\{\frac{\partial(\ln\dot{\varepsilon})}{\partial(\ln\sigma)}\right\}_T \tag{2}$$

Fig. 6 shows the logσ−1000/T curves of the alloy at different temperatures and at strain rate range of 1×10^{-3} s^{-1}

Table 1
Strain-hardening exponent obtained from the tensile tests.

Strain rate (s^{-1})	RT	200 °C	250 °C
1×10^{-1}	0.134	0.064	0.026
3×10^{-2}	0.133	0.056	0.023
1×10^{-3}	0.132	0.040	0.019

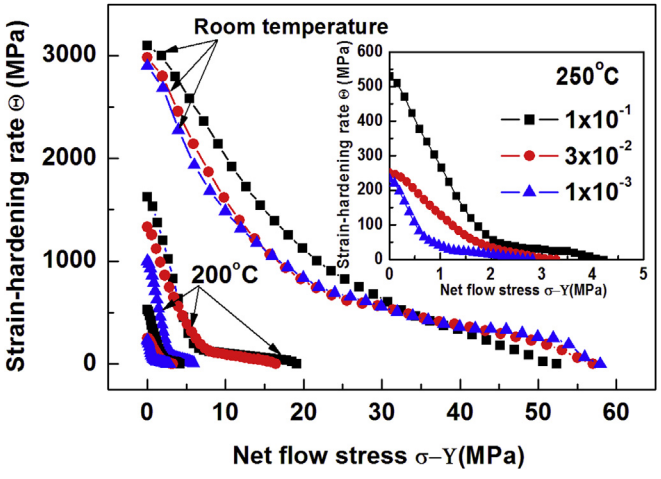

Fig. 5. Strain-hardening rate (Θ) as a function of net flow stress ($\sigma-Y$) of the alloy tested at room temperature, 200 °C and 250 °C, respectively.

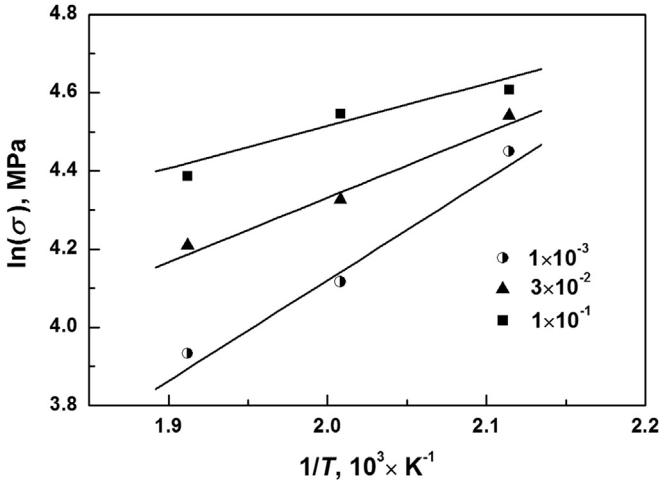

Fig. 6. Activation curves of ln(flow stress) vs. 1/T in deformation of the alloy.

to 0.1 s^{-1}, the corresponding Q values at different temperatures and strain rates can be obtained from the slopes of the $\log\sigma - 1000/T$. The Q value of the alloy is determined to be about 213.67 kJ mol^{-1} at 250 °C and a strain rate of 1×10^{-3} s^{-1}, which is higher than the activation energy for lattice diffusion (134 kJ mol^{-1}) or grain boundary self-diffusion (90 kJ mol^{-1}) obtained in other Mg alloys [33].

4. Discussions

4.1. Strain hardening behavior

The true stress-strain curves of the investigated alloy during uniform deformation indicate the evident strain hardening behavior. The variation of strain hardening ability with temperature and strain rate can be characterized by the strain hardening exponent (n) and the strain hardening rate (Θ). It can be seen from Fig. 2 that the effect of temperature on the strain hardening behavior is much greater than that of strain rate. So, the following discussions mainly consider the effect of temperature on the strain hardening behavior. As mentioned above, the values of n and initial Θ significantly decrease, but the elongation to failure remarkably increase with increasing temperature and decreasing strain rate (see Figs. 2 and 5). The results are mainly related to grain size strengthening and dislocation hardening caused by the obstacles of non-dislocation (solid atoms and precipitates) and forest dislocations. A recent strain hardening model took into account both effects [34,35],

$$\sigma = \sigma_0 + \sigma_{HP} + \sigma_d \quad (3)$$

where σ_0 is the frictional contribution, $\sigma_{HP}(\sigma_{HP} = kd^{-1/2})$ is the Hall-Patch contribution and σ_d ($\sigma_d = M\alpha Gb\rho^{-1/2}$) is the Taylor dislocation contribution, ρ is dislocation density, α is a constant, M is the Taylor factor, G is the shear modulus and b is the dislocation Burgers vector. Thus, it is necessary for the investigated alloy to observe its microstructure before and after tension to further evaluate the two strengthening effects.

Fig. 7 shows the TEM micrographs, HRTEM lattice images of the dislocations in Mg matrix and the corresponding IFFT images of tensile specimens of the alloy before and after tension at different temperatures with a strain rate of 1×10^{-3} s^{-1}, respectively. As shown in Fig. 7(a)–(d), the grain size of the alloy slightly increases with increasing testing temperature, while the scale, distribution and morphology of those particles do not change after tension. The alloy has a quietly clear grain boundary before tension, and the grain boundary appears ambiguous after tension at room temperature and 200 °C then becomes clear again at 250 °C. The HRTEM micrograph of the dislocations in the Mg matrix and the corresponding inverse fast-fourier-filtered (IFFT) image in Fig. 7 indicate the amount of dislocations in specimen after tension in Fig. 7(b) at room temperature is clearly higher than that before tension in Fig. 7(a). The corresponding dislocation densities in above two states are estimated to be $4.2 \times 10^{13}/m^2$ and $2.5 \times 10^{13}/m^2$, respectively. Therefore, the alloy has a high dislocation density and the obvious lattice distortion is also observed in Fig. 7(b) after tension at room temperature. Also, some dislocations occur to intersect in the Mg matrix and around second phase, which results in an increase of the dislocation density due to the dislocation multiplication [36]. Therefore, the alloy exhibits slightly high Θ and n at room temperature. Moreover, it can be seen that in addition to the change of grain boundary morphology, the number of dislocations in Mg matrix significantly decreases, while the grain size of alloy slightly increases with increasing testing temperature. This is mainly related to the formation, movements and intersection of dislocations. Under the force stress, a great number of dislocations present around those particles, at triple points and grain boundaries of the alloy. Parts of the dislocations will be pinned by the solute atoms or fine particles and bowed, and then form the dislocation loops due to local stress field. This causes the formation of new dislocations by the dislocation multiplication, and thus the dislocation density of the alloy will increase after tension. However, with increasing temperature, these dislocations annihilate mutually with dislocations of opposite sign approaching on closely glide planes (see the IFFT image of Fig. 7(d)) [37]. The dislocation annihilation leads to a decrease of dislocation density and further lowers the Θ and n of the alloy at 200 °C and 250 °C as shown in Fig. 5. The dislocation hardening caused by the multiplication, intersection and annihilation of dislocation is mainly responsible to the temperature dependence of the tensile strength, i.e., the tensile strength gradually decreases with increasing testing temperature, and this tendency can be explained by the change of dislocation density in α-Mg matrix. In addition, the dislocation structure also occurs to change during the elevated temperature deformation. The non-basal slip systems of prism and pyramidal types are activated due to the lower CRSS at high temperature [38]. Therefore, the elongation to failure of the alloy significantly increases with increasing temperature. Simultaneously, the average grain size of the alloy slightly increases from room temperature to 200 °C and 250 °C because of the grain boundary diffusion caused by the thermally activated dislocation movements. This

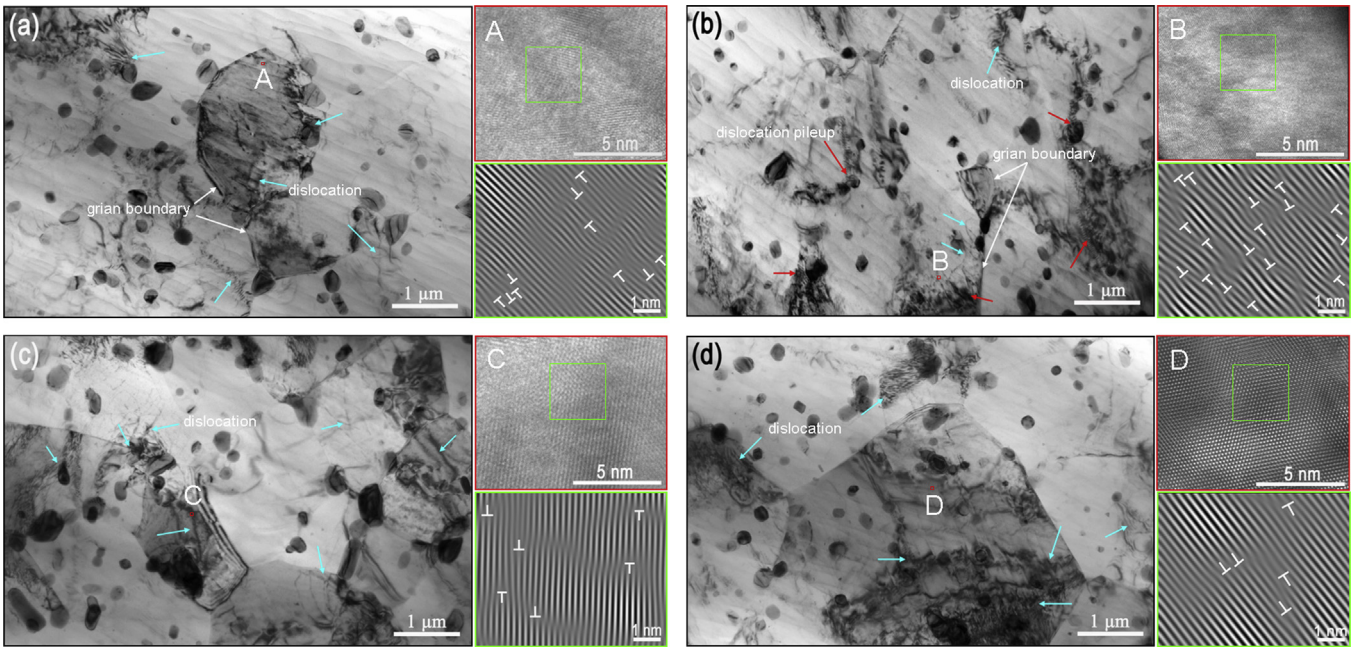

Fig. 7. TEM images of tensile specimens of the alloy before (a) and after tension at room temperature (b), 200 °C (c) and 250 °C (d) with a strain rate of 1×10^{-3} s^{-1}, HRTEM lattice images of the dislocations in the red regions marked by A, B, C and D in Mg matrix and corresponding IFFT images of the green areas in A, B, C and D.

is also another aspect to increase elongation to failure and decrease the strain hardening rate according to Eq. (3).

Interestingly, it is found that there is not the II-stage for the present alloy in the Kocks–Mecking type plot, but only III-stage and IV-stage indeed occur at room temperature (see Fig. 5). This is mainly related to low dislocation density. The similar experimental results are also reported in a friction stir welded Mg alloys [39]. As far as we know, the II-stage linear hardening behavior is a thermal in nature. The presence of the II-stage is due to the interaction of dislocation in the primary slip system with those in an intersecting slip system [40,41]. The dislocation interaction mainly depends on the dislocation density. For our alloy, the dynamic recrystallization sufficiently proceeds during hot extrusion, which accelerates the dislocation intersection and improves the probability of dislocation annihilation. Many dislocations created during cold work and stored in the basal alloy interacts each other, most of which just only take part in dislocation annihilation rather than multiplication, which finally results in the low dislocation density. Thus, the II-stage liner hardening is not appears in the Kocks–Mecking type plot.

4.2. Plastic deformation behavior

As mentioned in Section 3.4, the value of m is only 0.015 at room temperature then increases from 0.05 at 200 °C to 0.1 at 250 °C. The increased m value indicates that there exists a transition of deformation mechanism. The dominant deformation mechanism of the alloy is dislocation slip at room temperature, whereas the climb-controlled dislocation creep dominates the whole deformation process at 200 °C, and it transforms to grain boundary sliding mechanism at 250 °C [42]. This can be demonstrated by the surface observation of the fractured tensile specimens at the different temperatures under a strain rate of 1×10^{-3} s^{-1} as shown in Fig. 8. At room temperature, some macro-cracks are observed in the surface of fractured tensile specimen, which intersect each other at about 45° (see Fig. 8(a)). A large number of fine rod-like Mg_2Sn particles and the irregular $Mg_2(Sn,Yb)$ particles distribute along tensile direction. The micro-cracks as shown in Fig. 8(b) initiate at the phase interface between these second phases and α-Mg matrix due to the stress concentration caused by dislocation pileup (see red arrows in Fig. 7(b)). The formation of macro-cracks in Fig. 8(a)–(c) is attributed to the growth and coalescence of those micro-cracks. By careful observation, some shear bands form at the grain boundary, indicating the weaker grain boundary compatibility of the alloy at room temperature [43]. This demonstrates that the deformation mechanism is only controlled by dislocation slip rather than the grain boundary sliding. In addition, the high n value (0.134) and low m value (0.015) suggest the alloy has good strain hardening ability and poor uniform plastic deformation behavior. Thus, the alloy exhibits the low elongation to failure (10%) at room temperature.

Oppositely, as compared with that at room temperature, the fractured tensile specimens of the alloy appear the obvious necking at 200 °C and 250 °C (see Fig. 8(d) and (g)). As far as we know, the strain rate sensitivity can characterize the capacity to resistant necking, and indicate the ability to undergo superplastic deformation of the alloy. The high m value can improve the necking resistance and stop the alloy from locally fracturing due to stress concentration. Therefore, the elongation to failure of the alloy significantly increases with increasing m value, whose highest value reaches 100.2% at 250 °C with a strain rate of 1×10^{-3} s^{-1}, indicating a quasi superplastic behavior. At this moment, the surface of the alloy

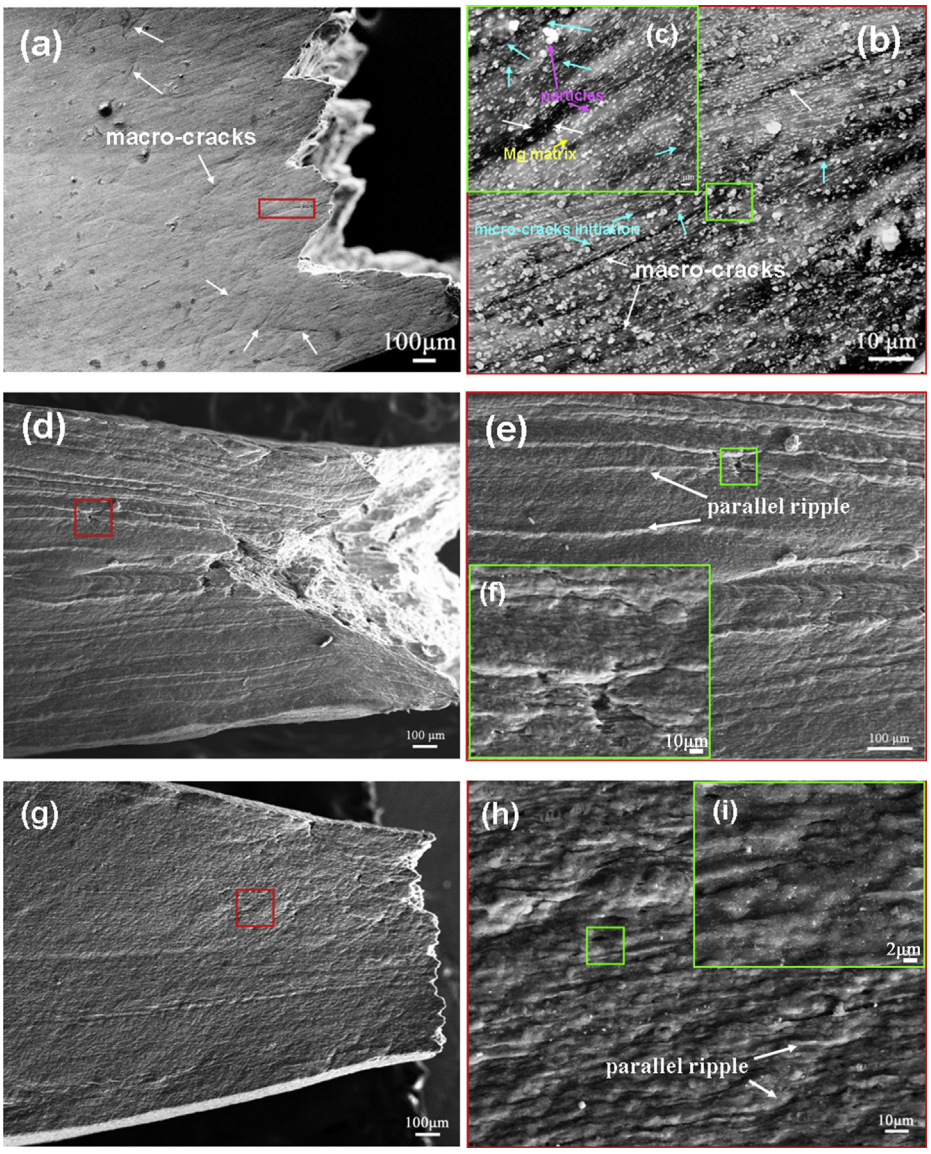

Fig. 8. Macroscopic surface (a), (d) and (g) of the broken tensile specimens and the deformed surface at low magnification as marked with the red frame (b), (e) and (h) and high magnification as marked with the green frame (c), (f) and (i) at a strain rate of $1 \times {}^{10-3}$ s^{-1} at room temperature, 200 °C and 250 °C, respectively.

trends to be flat and a small number of fine global cavities are observed in the region next to the fracture surface at the interface between the Mg matrix and second phase particles (see Fig. 8(f) and (i)). These cavities with large size mainly distribute along tensile direction. The formation of those microcavities in the fractured tensile specimen surface usually means the operation of grain boundary sliding and grain rotation in Mg alloys with superplasticity [44]. In addition, some parallel ripple marks are observed in the fractured tensile specimen surface (marked by white arrows in Fig. 8(e) and (h)), which can also confirm the occurrence of grain-boundary sliding [45]. In general, the grain boundary sliding occurs readily, but often is blocked and inhibited at triple points or grain boundary ledges. However, the generation of dislocation can remove these impediments [32]. In this paper, it can be seen from Fig. 7(b)–(d) that the size of most of particles (Mg_2Sn and $Mg_2(Sn,Yb)$) does not significantly increase and the distribution of those particles become more homogenous as shown in Fig. 7(d). Although only small amounts of particles occur to slightly coarsen as seen in Fig. 7(c), this does not affect the effect that those particles inhibit the dislocation gliding or climbing, especially at elevated temperature. Meanwhile, theses particles can further block GBS, the dislocation is hard to get across those phase boundaries, and therefore the activation energy for quasi superplastic flow is much higher than that of grain boundary diffusion or lattice diffusion of magnesium alloys. The similar phenomenon is also reported in other Mg alloys with superplasticity [43,46]. In addition, these particles at the grain boundaries cause the retardation of grain growth, and the grain size of the alloy only slightly increases at elevated temperature (see Fig. 7(c)). The formation of quasi superplasticity of the alloy is associated with the fine microstructure and presence of the Mg_2Sn and $Mg_2(Sn,Yb)$ particles.

5. Conclusions

(1) The Mg−2Sn-0.5Yb alloy sheet exhibited the high strain-hardening ability at low temperature and high strain rate. The values of n and Θ of the alloy decreased with increasing testing temperature and decreasing strain rate. Kocks−Mecking type plots showed that the alloy did not exhibit II-stage at room temperature, and III-stage and IV-stage subsequently occurred after yielding, especially at higher temperature. This is mainly related to the change of dislocation density before and after tension.

(2) The deformation mechanism of alloy occurred to change at different temperatures. The dominant deformation mechanism of the alloy was dislocation slip at room temperature, whereas the climb-controlled dislocation creep dominated the whole deformation process at 200 °C, and it transformed to grain boundary sliding mechanism at 250 °C. The value of m of the alloy increased with increasing testing temperature. The corresponding m-value and activation energy were calculated as 0.1 and 213.67 kJ mol^{-1}, respectively. In addition, the alloy exhibits a quasi superplasticity at 250 °C with a strain rate of 1×10^{-3} s^{-1}, which is mainly related to the fine microstructure and the presence of the Mg_2Sn and Mg_2(Sn,Yb) particles.

Acknowledgments

This work was financially supported by the National Nature Science Foundations of China (No. 51371089 and No. 51301082).

References

[1] B.L. Mordike, T. Ebert, Mater. Sci. Eng. A 302 (2001) 37−45.
[2] H. Somekawa, H. Hosokawa, H. Watanabe, Mater. Sci. Eng. A 339 (2003) 328−333.
[3] K. Kitazono, E. Sato, K. Kuribayashi, Scr. Mater. 44 (2001) 2695−2702.
[4] Q.M. Peng, Y.D. Huang, K. Kainer, N. Hort, Mater. Lett. 83 (2012) 209−212.
[5] J.H. Zhang, S.J. Liu, Z. Leng, X.H. Liu, Z.Y. Niu, M.L. Zhang, R.Z. Wu, Mater. Sci. Eng. A 531 (2012) 70−75.
[6] M.S. Dargusch, S.M. Zhu, J.F. Nie, G.L. Dunlopc, Scr. Mater. 60 (2009) 116−119.
[7] U.F. Kocks, H. Mecking, Prog. Mater. Sci. 48 (2003) 171−273.
[8] R. von Mises, Z. Angew. Math. Mech. 8 (1928) 161−185.
[9] Z. Trojanov á, P. Lukáč, J. Mater. Process. Technol. 162−163 (2005) 416−421.
[10] X.H. Chen, L. Lu, Scr. Mater. 67 (2007) 133−136.
[11] H.Y. Wu, F.Z. Lin, Mater. Sci. Eng. A 527 (2010) 1194−1199.
[12] H.Y. Wang, X.L. Nan, N. Zhang, C. Wang, J.G. Wang, Q.C. Jiang, Mater. Chem. Phys. 132 (2012) 248−252.
[13] Y.H. Zhao, X.Z. Liao, S. Cheng, E. Ma, Y.T. Zhu, Adv. Mater. 18 (2006) 2280−2283.
[14] M. Knezevic, A. Levinson, R. Harris, R.K. Mishra, R.D. Doherty, S.R. Kalidindi, Acta Mater. 58 (2010) 6230−6242.
[15] A.A. Salem, S.R. Kalidindi, R.D. Doherty, Acta Mater. 51 (2003) 4225−4237.
[16] F. Qiu, P. Shen, Z.H. Jiang, T. Liu, Q.C. Jiang, Appl. Phys. Lett. 92 (2008), 151912−;151912−3.
[17] C.R. Brooks, Heat Treatment, Structure and Properties of Nonferrous Alloys, American Society for Metals, Metals park, OH, USA, 1982, p. 261.
[18] H.K. Lim, D.H. Kim, J.Y. Lee, W.T. Kim, D.H. Kim, J. Alloys Compd. 468 (2009) 308−314.
[19] H.D. Zhao, G.W. Qin, Y.P. Ren, W.L. Pei, D. Chen, G. Yun, Trans. Nonferrous Met. Soc. China 20 (2010) s493−s497.
[20] G. Nayyeri, R. Mahmudi, Mater. Sci. Eng. A 527 (2010) 2087−2098.
[21] M. Keyvani, R. Mahmudi, G. Nayyeri, Metall. Mater. Trans. A 42 (2011) 1990−2003.
[22] M. Keyvani, R. Mahmudi, G. Nayyeri, Mater. Sci. Eng. A 527 (2010) 7714−7718.
[23] Do H. Kim, H.K. Lim, Y.K. Kim, J.S. Kyeong, W.T. Kim, D.H. Kim, Met. Mater. Int. 17 (2011) 383−388.
[24] C. Dharmendra, K.P. Rao, Y.V.R.K. Prasad, N. Hort, K.U. Kainer, Mater. Chem. Phys. 136 (2012) 1081−1091.
[25] K.P. Rao, Y.V.R.K. Prasad, K. Suresh, N. Hort, K.U. Kainer, Mater. Sci. Eng. A 552 (2012) 444−450.
[26] C. Dhar mendra, K.P. Rao, Y.V.R.K. Prasad, N. Hort, K.U. Kainer, J. Mater. Sci. 48 (2013) 5236−5246.
[27] S.S. Park, B.S. You, Scr. Mater. 65 (2011) 202−205.
[28] H. Liu, Y. Chen, Y. Tang, Y. Tang, S. Wei, G. Niu, Mater. Sci. Eng. A 464 (2007) 124−128.
[29] S. Wei, Y. Chen, Y. Tang, X. Zhang, M. Liu, S. Xiao, Y. Zhao, Mater. Sci. Eng. A 508 (2009) 59−63.
[30] J. Jiang, G.L. Bi, J.A. Liu, C.C. Ye, J.S. Lian, Z.H. Jiang, J. Mater. Eng. Perform, (Submit).
[31] J. Luo, Z. Mei, W. Tian, Z. Wang, Mater. Sci. Eng. A 441 (2006) 282−290.
[32] X. Wu, Y. Liu, Scr. Mater. 46 (2002) 269−274.
[33] H.J. Frost, M.F. Ashby, Deformation Mechanism Maps, Pergamon Press, Oxford, 1982, p. 44.
[34] J.A. del Valle, F. Carreno, O.A. Ruano, Acta Mater. 54 (2006) 4247−4259.
[35] J.A. del Valle, O.A. Ruano, Scr. Mater. 55 (2006) 775−778.
[36] A.T. Thomas, Acta Mater. 14 (1966) 1363−1374.
[37] U. Essmann, H. Mughrabi, Philos. Mag. A 40 (1979) 731−756.
[38] J. Koikea, T. Kobayashia, T. Mukaib, H. Watanabeb, M. Suzukia, K. Maruyamaa, K. Higashic, Acta Mater. 51 (2003) 2055−2065.
[39] N. Afrin, D.L. Chen, X. Cao, M. Jahazi, Scr. Mater. 57 (2007) 1004−1007.
[40] C.H. Cáceres, A.H. Blake, Mater. Sci. Eng. A 462 (2007) 193−196.
[41] M. Srinivasan, T.G. Stoebe, J. Mater. Sci. 9 (1974) 121−128.
[42] L.B. Tong, M.Y. Zheng, D.P. Zhang, W.M. Gan, H.G. Brokmeier, J. Meng, H.J. Zhang, Mater. Sci. Eng. A 586 (2013) 71−77.
[43] J. Koike, R. Ohyama, T. Kobayashi, M. Suzuki, K. Maruyama, Mater. Trans. 44 (2003) 445−451.
[44] L. Li, X.M. Zhang, Y.L. Deng, C.P. Tang, J. Alloys Compd. 485 (2009) 295−299.
[45] X.H. Liu, H.B. Zhan, S.H. Gu, Z.K. Qu, R.Z. Wu, M.L. Zhang, Mater. Sci. Eng. A 528 (2011) 6157−6162.
[46] X.B. Liu, R.S. Chen, E.H. Han, Mater. Sci. Eng. A 497 (2008) 326−332.